HHS Public Access

Author manuscript

IEEE Trans Med Imaging. Author manuscript; available in PMC 2019 February 01.

Published in final edited form as:

IEEE Trans Med Imaging. 2018 February ; 37(2): 417–427. doi:10.1109/TMI.2017.2753739.

Magnetic Resonance Mediated Radiofrequency Ablation

Yik-Kiong Hue [Member IEEE],
Athinoula A. Martinos Center for Biomedical Imaging, Department of Radiology, Massachusetts General Hospital, Charlestown, MA, USAHarvard Medical School, Boston, MA, USA

Alexander R. Guimaraes,
Martinos Center, MGH and HMS

Ouri Cohen,
Martinos Center, MGH and HMS

Erez Nevo,
Robin Medical, Inc., Baltimore, MD 21203 USA

Abraham Roth, and
Robin Medical, Inc., Baltimore, MD 21203 USA

Jerome L. Ackerman
Martinos Center, MGH and HMS

Abstract

Objective—To introduce magnetic resonance mediated radiofrequency ablation (MR-RFA), in which the MRI scanner uniquely serves both diagnostic and therapeutic roles. In MR-RFA scanner-induced RF heating is channeled to the ablation site via a Larmor frequency RF pickup device and needle system, and controlled via the pulse sequence.

Methods—MR-RFA was evaluated with simulation of electric and magnetic fields to predict the increase in local specific-absorption-rate (SAR). Temperature-time profiles were measured for different configurations of the device in agar phantoms and ex vivo bovine liver in a 1.5 T scanner. Temperature rise in MR-RFA was imaged using the proton resonance frequency method validated with fiber-optic thermometry. MR-RFA was performed on the livers of two healthy live pigs.

Results—Simulations indicated a near 10-fold increase in SAR at the RFA needle tip. Temperature-time profiles depended significantly on the physical parameters of the device although both configurations tested yielded temperature increases sufficient for ablation. Resected livers from live ablations exhibited clear thermal lesions.

Conclusion—MR-RFA holds potential for integrating RF ablation tumor therapy with MRI scanning.

Correspondence to: Ouri Cohen.

Current affiliation: Yik-Kiong Hue, Intelligent Automation, Inc., Rockville MD, USA.
Current affiliation: A. R. Guimaraes, Department of Diagnostic Radiology, Oregon Health & Sciences University, Portland, OR, USA.

Index Terms

MRI; radiofrequency ablation (RFA); interventional radiology; liver cancer; proton resonance frequency (PRF) shift thermal imaging

I. INTRODUCTION

DURING the more than four decades that MRI has been in existence, it has served in a primarily diagnostic role, with substantially less utility in MRI-guided interventions. In this report, we introduce Magnetic Resonance Mediated Radiofrequency Ablation (MR-RFA) in which the MRI scanner assumes the role of a therapeutic device. More specifically, MR-RFA harnesses the RF heating effect of MRI excitation pulses—normally a safety risk—by directing the scanner's RF energy to the site of a tumor and thereby accomplishing thermal ablation [1]. A closely related methodology uses scanner RF heating to coagulate a thermosetting biomaterial for vascular repair [2], [3]. The MR-RFA concept is shown schematically in Fig. 1.

In therapeutic thermal tissue ablation [4]–[6] tissue is heated above 60°C, leading to protein denaturation and membrane breakdown which result in irreversible thermal damage [7], [8]. A common example, percutaneous radiofrequency ablation (RFA), introduced over two decades ago for the treatment of osteoid osteomas [9] and later for primary and metastatic liver tumors [10]–[12], gained attention because it is effective, safe, minimally invasive, low in cost and far less traumatic to the patient compared to surgery, chemotherapy or radiation therapy. Its application has been expanded to many other cancers [13]–[16].

Successful ablation requires image guidance for placement of the RFA needle (RF applicator). Several imaging modalities may be used but MRI is especially attractive since it exhibits high soft tissue contrast (sometimes without the use of an exogenous contrast agent), is non-ionizing, and is capable of imaging tissue temperature and other thermal effects [17], [18] in near real-time [19], [20]. The benefits of MRI guidance are offset, however, by its cost and by the requirement for MR-compatible RFA equipment. The RFA apparatus must operate safety in the presence of the static, gradient and RF magnetic fields of the scanner, and must not introduce noise or distortion into the images [21], [22]. The RFA generator in particular can create electrical interference with MR image acquisition [23] and must therefore be placed away from the scanner and connected via RF-filtered MR-compatible cables. Image artifacts from conventional RFA equipment can be mitigated by alternating heating with MR imaging to avoid interference but at the cost of reduced heating efficiency caused by heat transport via tissue perfusion that may lead to inadequate ablation In principle, MR-RFA can image and heat simultaneously.

MR-RFA does not require an external RF power generator or electrical connections to any external system. The ablation device has minimal circuitry and does not require a grounding pad to complete the electrical path, eliminating the possibility of accidental skin burns [24]–[30] due to poor contact between the grounding pad and the skin. Although the occurrence of severe third-degree burns is estimated to be on the order of a few percent, milder burns are believed to occur in as much as 33% of cases; burn incidents are probably underreported

[28]. It enables tight interleaving or simultaneity of heating and diagnostic functions. Although the specific absorption rate (SAR) estimated by the scanner is intended to reduce the risk of excessive tissue heating, it is nevertheless possible to create localized “hot spots” by placing conductive structures in the RF coil. The MR-RFA method captures RF energy from the transmit coil and directs it to intentionally created zones of tissue heating by means of passive conductive devices alone, enabling MRI guidance and monitoring simultaneous with RF heating. This report demonstrates the feasibility of MR-RFA using simulations and experiments in phantoms, tissue specimens and healthy live domestic swine.

A major drawback of conventional RFA is the relatively high rate of local recurrences in treated lesions (20–50% depending on tumor size and location) [31], [32]. The reasons for local recurrences include inability to identify the zone of ablation created relative to the location of the tumor and the location of the tumor/normal boundary; inability to confirm coagulation necrosis during treatment; inaccurate placement of electrodes when the intent is to ablate larger tumors by overlapping zones of ablation; and thermoprotection of tumor cells along major blood vessels, which serve as heat sinks to keep adherent tumor cells at lower, non-lethal temperature levels. Another drawback of conventional RFA is the inability to noninvasively monitor the temperatures of the treated tissues in real time.

The difficulties described in the last paragraph have solutions achievable through various means. Skin burns may be reduced with split or sequentially activated grounding pads. Conventional RFA may be conducted in an MRI scanner to image tissue temperature [33]–[38] (“MRI-guided RFA”), In contrast to MRI-guided RFA, MR-RFA holds potential to improve conventional RFA by eliminating the external RFA generator and grounding pads, while integrating the diagnostic and ablation functions in a single instrument which in principle could be automated to produce a specified temperature increase in a target tissue volume thereby addressing some (but not all) of the causes of local tumor recurrence. In this demonstration-of-concept study there was no attempt to define or create an optimal ablation zone.

II. THEORY

MR-mediated RF ablation employs Faraday induction to couple RF energy from the scanner’s body RF coil to a conductive device (e.g., a wire) connected to a needle inserted into the treatment zone. The effectiveness of the wire’s power transfer efficiency depends on its electrical network properties, the Larmor frequency, and the relative geometry of the wire and the scanner transmit coil. Much like a wire moving in a static magnetic field generates an electromotive force (EMF) along its length (Fig. 2a), the rotating magnetic flux from the circularly polarized body RF coil cutting across a stationary wire also generates an EMF (Fig. 2b). Unlike conductors in an electric power generator operating at 50 or 60 Hz, the wire’s length is on the order of the RF wavelength, and therefore must be treated as a resonant structure (an antenna or a transmission line) supporting standing waves. Dielectric and inductive heating will occur in tissue adjacent to the wire because of the electric and magnetic fields along the wire’s length, and ohmic heating will occur from current flow into the tissue at the wire’s tip. Unlike conventional RFA, where the operating frequency is typically below 1 MHz, and a return current path (the grounding pad) is required to complete

the electrical circuit, the current return path in MR-RFA may be thought of as the electromagnetic coupling between the body RF coil, the wire and the subject. In MR-RFA a physical grounding pad, with its risk of skin burns, is therefore not required. Because the return path is distributed over a large surface area (and as long as potentially dangerous localized hot spots are avoided), the return current density is low and heating from this source is minimal.

Viewing the wire as the secondary winding of an RF transformer, the wire itself can be treated as a resonant transmission line which should be tuned to the Larmor frequency for optimum power coupling, and which should be impedance matched to the load (the RFA applicator embedded in tissue). This suggests that the wire length be a multiple of half wavelengths. However, the electrical length of this transmission line is proportional to the inverse square root of the dielectric constant of medium surrounding the wire, which ranges over an order of magnitude as the wire is routed through air, past various insulating materials, and ultimately adjacent to and embedded in tissue. Therefore, the effective electrical length of the wire is challenging to control, and will vary as the wire and RFA applicator are manipulated by the surgeon during the procedure. Likewise, viewing the wire as an antenna leads again to the conclusion that its length should be close to half wave (the basic dipole antenna), but this is rigorously true only in free space. The environment of this “antenna” is drastically altered by the wide ranging and time-dependent electrical properties of materials in the environment in which the antenna is embedded. Although viewing the wire in simplified conceptual terms as either a transmission line or antenna helps with basic understanding and guidance in its use, a full numerical simulation of its electromagnetic behavior is required for a deeper understanding of its performance and optimization.

A simple description of the underlying physics, applicable to a homogeneous medium, follows. This description is locally valid for limited lengths of the wire; the geometric and tissue electrical parameters will vary with position along the wire.

Assuming a wire of length l completely immersed in the B_1 field, and placed parallel to the magnet axis at radius r from the center of the magnet bore with one end in contact with the sample tissue, the induced distributed EMF for the part of the wire subject to the magnetic flux can be calculated as:

$$\mathrm{EMF}=r\omega B \quad (1)$$

where ω is the angular frequency of the scanner and B is the component of the magnetic flux density perpendicular to the wire. The current $I(z)$ and the voltage $V(z)$ on the line at position z satisfy the inhomogeneous Helmholtz equation which can be solved using the Green’s function method [39] to yield:

$$I(z) = (j\omega C+G)\int_0^l g\left(z, z'\right) f\left(z'\right) dz' \quad (2)$$

$$V(z) = -\int_0^l \frac{dg\left(z, z'\right)}{dz} f\left(z'\right) dz' \quad (3)$$

where $g(z, z')$ is the Green's function, f is the EMF source, and C and G are the respective capacitance and conductance per unit length. Setting the boundary conditions $I(0) = 0$ and $V(l)/I(l) = Z_L$, where $I(0)$ is the current at the free end of the wire (viewed in its environment as a transmission line), Z_L is the tissue impedance at the load (wire tip immersed in tissue), and γ is the complex propagation constant [40], the Green's function solution is given by:

$$g\left(z, z'\right) = \frac{1}{2\gamma\left(e^{\gamma l} + \Gamma_L e^{-\gamma l}\right)} \times \begin{cases} \left(e^{-\gamma l} - e^{\gamma l}\right)\left(e^{-\gamma\left(z'-l\right)} - \Gamma_L e^{\gamma\left(z'-l\right)}\right) & z < z' \\ \left(e^{-\gamma z'} - e^{\gamma z'}\right)\left(e^{-\gamma\left(z'-l\right)} - \Gamma_L e^{\gamma(z-l)}\right) & z > z' \end{cases} \quad (4)$$

The symbol Γ_L is the complex reflection coefficient at the end of the wire:

$$\Gamma_L = (Z_L - Z_0) / (Z_L + Z_0) \quad (5)$$

where Z_0 is the characteristic impedance of the line and a, b denote the boundaries of the wire. The current at the tip of the wire can hence be approximated as:

$$I_L \approx \frac{\omega r B\left(\Gamma_L - 1\right)}{\gamma Z_0\left(e^{\gamma l} + \Gamma_L e^{-\gamma l}\right)} \left(cosh\left(\gamma b\right) - cosh\left(\gamma a\right)\right) \quad (6)$$

The propagation constant γ is given by:

$$\gamma = \sqrt{(R + j\omega L)(G + j\omega C)} \quad (7)$$

where R and L are the respective series resistance and inductance per unit length.

Unlike in conventional transmission lines, all of the line parameters L, C, R, and G, as well as the derived parameters Z and γ (or alternatively, the electrical wavelength) are functions of position of the wire, position along the wire, and time. R and G, representing RF power loss and thus tissue heating, can be significantly different from zero.

An alternative means to capture RF energy from the transmit coil of the scanner is to use a resonant loop, in effect a surface coil used in reverse. The loop is tuned to the Larmor frequency, impedance matched to the transmission line (wire), and positioned against the magnet bore in a suitable position. If the loop is the dominant source of RF energy pickup, the positioning of the wire becomes less critical.

III. METHODS

A. Simulation

Rather than attempt an analytical treatment, the MR-RFA system was modeled numerically using the finite difference time domain method with the XFDTD 7.0 (Remcom Inc., State College, PA) software package. A model of a 16-rung high-pass birdcage body RF coil 60 cm long and 60 cm diameter, enclosed in a 110 cm long, 70 cm diameter perfect electrical conductor (PEC) shield, was defined, as was a model of a Siemens body loader centered in the coil (Fig. 3a). The quadrature transmit/receive ports of the coil are at the 4:00 and 7:00 o'clock positions in this and subsequent figures. The simulation grid step size (spatial resolution for the computation) was chosen to be 1 cm and the model was contained within a 70 cm × 70 cm × 150 cm volume.

A Gaussian pulse with a −60 dB cutoff at 250 MHz was used to excite all the operating modes of the high-pass birdcage coil. The highest frequency operating mode (uniform B_1) was identified by checking the homogeneity of the magnetic field within the spherical phantom of the Siemens body loader and the decoupling of the two ports. This mode was then tuned to the Larmor frequency by adjusting the end ring capacitors.

A 31 cm × 23 cm × 7 cm rectangular solid representing the liver centered in the coil, with the electrical properties of liver tissue (dielectric constant 70.62, conductivity 0.55 S/m [41]), then replaced the body loader, and the simulation run again. The electric field computed from the simulation was sampled along the edges of each FDTD Yee cell in the simulated liver. Using MATLAB (The Mathworks, Natick, MA, USA) for post-processing, each component of the electric field at the center of the cell was computed from the average of the corresponding components of the four electric fields surrounding the cell. The square of the electric field vector magnitude was computed to display the SAR map [42].

Finally, the wire, modeled as a perfect electrical conductor (PEC) looping through the central volume and with its tip immersed 4 cm in the liver phantom to approximate the experimental configuration, was added to the geometry, and the simulation run once more. The geometry of the simulated liver and wire in the RF coil appears in Fig. 3b.

B. Temperature measurement and MR thermometry

To demonstrate that MR thermometry can be carried out in the vicinity of the needle despite its intense coupling to the body RF coil and the strong intensity artifact, images of the temperature increase following heating were recorded using the proton resonance frequency (PRF) method [43]. Single slice GRE phase images of duration 3.4 s were recorded immediately before and after heating. The phase of each image was unwrapped using an adaptation of the Jenkinsen phase unwrapping algorithm [44] programmed in MATLAB. Spatial regions of the image above a certain intensity threshold were clustered depending on the range of phase values, with the ranges chosen small enough such that there is no phase rollover within a cluster. Adjacent clusters are compared and conditionally combined depending on their relative phase, and whether wrapping around 180° is required. The process is repeated until only a single cluster remains. The phase difference between the before and after images is scaled to yield the temperature change.

Continuous monitoring of the wire tip temperature was provided by a Neoptix (Québec City, QUE, Canada) T1 fiber optic temperature probe affixed to the wire about 5 mm behind the tip with Teflon tape. The temperature probe was connected to a Neoptix Reflex signal conditioner. Temperaturetime profiles were recorded using the serial interface of the signal conditioner. Cadaver and live ablations performed with a homebuilt hollow brass needle connected to the wire were recorded with a Luxtron (LumaSense Technologies, Inc., Santa Clara, CA, USA) fiber optic temperature probe inside the needle because of the smaller diameter of the Luxtron optical fiber.

C. MRI

Experiments were conducted primarily on a Siemens (Erlangen, Germany) Avanto 1.5 T scanner. Some experiments were conducted on a Siemens Trio 3.0 T scanner to examine the effects of Larmor frequency. A high RF duty cycle turbo spin echo (TSE) heating sequence consisting of one 90° pulse and three 150° pulses with repetition time (TR) of 643 ms was typically used to ensure sufficient heat deposition. Imaging was done with a gradient-echo (GRE) sequence with FA/TR/TE/BW = 25°/381 ms/4.8 ms/260 Hz/pixel with a matrix of 128 × 128 × 45 and a resolution of 4 mm × 4 mm × 7.5 mm. Phase maps for the temperature measurements were acquired with a single slice GRE sequence with the same acquisition parameters except that TR/TE = 13.8 ms/10 ms. The phase images resulted in negligible heating.

D. Phantom testing

Wire pickup—Teflon insulated silver plated 26 gauge solid wire (Alpha Wire Company, Elizabeth, NJ, USA) of varying lengths (1.4–2.2 m) was stripped to expose 5 mm of the conductor at the tip. The exposed tip with the fiber optic temperature probe affixed was inserted into a 25-liter saline 1% agar gel phantom composed 5.0 g/L NaCl (Thermo Fisher Scientific, Waltham, MA, USA), 1.25 g/L $NiSO_4 \cdot 6H_2O$ (Thermo Fisher), and 10 g/L agar (Sigma Aldrich, St. Louis, MO, USA) to simulate the electrical and MR relaxation properties of tissue. The length of the wire was looped around the head end of the patient table and taped to its upper surface at its edges so that it was positioned at the maximum possible radius. The temperature-time profile was measured for each individual wire length. Given the 57 cm length of the body coil, only a fraction of the wire length was completely inside the body coil. To avoid effects due to gel damage and local compositional changes from repeated heating experiments, the wire's location in the gel was changed to a fresh unperturbed location after each heating sequence.

In subsequent experiments a means was developed to provide adjustment of the electrical properties of the wire to compensate for differences in the wire path in the scanner. To provide fine adjustment of the wire's electrical length, a Sprague-Goodman (Westbury, NY, USA) SGNMNC3708E nonmagnetic high voltage 3–70 pF 78–turn variable capacitor was placed in series with the wire. The capacitor was equipped with a 100-turn digital readout dial and mounted in a plastic enclosure. Adjustment of the capacitor permitted the heating rate to be optimized for a particular layout of the wire. The wire configuration was used for all experiments other than the phantom experiments.

Loop pickup—To measure the impact of the loop's size on the heating profile, two square loop circuits with sizes 11 cm × 11 cm and 19 cm × 19 cm were built using 5 mm wide copper adhesive tape on ABS sheet, nonmagnetic high voltage fixed ceramic chip (American Technical Ceramics, Huntington Station, NY, USA) and Sprague variable capacitors, and tuned to the 64 MHz Larmor frequency of the scanner. A length of Temp-Flex (South Grafton, MA, USA) 50HCX-15 high temperature nonmagnetic Teflon-insulated 1.8 mm diameter 50 ohm coaxial cable connected the pickup loop to the enclosed series variable capacitor (in essence, the impedance matching capacitor). An additional length of cable, with 5 mm bare center conductor exposed and the fiber optic temperature sensor affixed, was inserted into the gel phantom.

E. Bovine liver tissue

The performance of MR-RFA was tested in bovine liver purchased at a local grocery store. A 3.4 m 26 gauge wire was connected to a 15 cm long 16 gauge bare copper wire which was used as the RF applicator to induce lesions in the liver tissue. Ablations were conducted at 1.5 T. This wire length had been found to maximize the heating for this particular wire configuration at this field. To compare the ablation lesions created by MR-RFA with conventional RFA, several ablation lesions were created out of the MRI scanner in one piece of liver tissue with a Valleylab Cool-tip RF Ablation System (Covidien/Medtronic, Minneapolis, MN USA) operating at 480 kHz. The tissue was placed in an aluminum pie pan serving as the grounding pad. As in the MR-RFA tests, no saline cooling was used. This ablation was carried out by an experienced radiologist who routinely treats patients with RFA.

F. Pig cadavers

Two Yorkshire domestic swine cadavers, which were discarded following other experiments that left the livers intact, underwent MR-RFA using the wire RF pickup system at 1.5 T. The ablations were carried out using the hollow needle RF applicator which could be inserted through the chest wall into the liver.

G. Live pigs

All experiments were approved by the Partners Healthcare Institutional Animal Care and Use Committee and conducted in accordance with its guidelines. The clinical feasibility of the proposed device for use in liver ablation was tested in an *in vivo* porcine model at 1.5 T. Two healthy domestic Yorkshire swine were anesthetized by IM injection with Telazol 4.4 mg/kg, xylazine 2.2 mg/kg and atropine 0.05 mg/kg and transported to the Martinos Center. There they were intubated, and maintained under general anesthesia for the duration of the MR-RFA procedure with 1–2% isoflurane, 50% N_2O, balance O_2, with periodic monitoring of arterial blood gases, pulse oximetry respiration rate, and blood pressure. The RFA needle was positioned in the animal's liver by a trained interventional radiologist with over 5 years of experience in percutaneous image guided procedures. Although the needle creates strong intensity artifacts, the abdominal anatomy is still clearly visible. Successive anatomic scans were acquired as the needle was advanced, and a final scan confirmed that the needle tip as visualized by the artifact entered the liver. No real-time procedures were used. Three initial

anatomical scans with slice directions along the A-P, S-I and R-L axes confirmed the position of the RFA needle tip in the liver. MR thermometry scans were not performed because of the lack of motion-compensated thermometry pulse sequences on this scanner. Following needle insertion the ablation was initiated with a TSE heating sequence. This procedure was repeated at three different liver locations, following which the animal was euthanized and the liver removed en bloc. The liver was sectioned and the site photographed to record the size and shape of the lesions.

IV. RESULT

A. Simulation

The simulated coil was tuned to 64.1 MHz, close to the Larmor frequency, with rung capacitors of 100 pF. The return loss for ports 1 and 2 was −25 and −23 dB respectively, and the coupling between the quadrature ports was −30 dB, showing good isolation. The inhomogeneity of the simulated B_1^+ field within the FOV (spherical volume defined in the body loader) of the unloaded coil was less than 5%. Fig. 4 shows the simulated B_1^+ RF field contour plots for the unloaded (a) and body loaded (b) coil at the transverse midplane. Cross sections of the B_1^+ field with the simulated liver without (Fig. 4c) and with (Fig. 4d) the RFA wire present are shown in the lower panels. Only the final turn of the wire and its tip inserted into the liver are captured in the displayed central slice. Note that because of its conductivity, the presence of the liver alone affects the homogeneity of B_1^+ to a modest degree.

Including the RFA wire significantly distorts the B_1^+ field. The wire itself carries a strong B_1^+ component. Although the wire has zero width in the model geometry (it is represented as lying on cell boundaries), the computational result is for complete Yee cells, and therefore the wire's width appears to be magnified to at least full cell width. Furthermore, to restrict the dynamic range of the contour plot representation so that the homogeneity of the field is readily visualized, B_1^+ values are limited to 2× the central field in Fig. 4a. The peak field at the wire is far greater than this limit, further adding to the apparent width of the wire.

The behavior of the electric field is noteworthy. Fig. 5 displays the SAR (electric field squared magnitude) as a color plot within the simulated liver. The liver without the wire is portrayed in the upper panel (a), while the liver containing the wire tip appears in the lower panel (b). Without the wire present, the electric field is relatively uniform, with a small increase in field at the air boundaries at the edges of the color map. As expected, the SAR was maximal at the tip of the wire (at 0 cm on the vertical axis). The field at the tip is 9.7 × that of the maximum field in the unperturbed liver, creating an intense hot spot. Despite this localized effect on SAR, the overall effect on the phantom is modest. Including the wire increases the return loss (detunes the RF coil) such that the total power deposition in the phantom is only 44% that when the wire is not present. The wire concentrates power deposition primarily at its tip.

B. MR thermometry

The hollow brass RFA needle creates a substantial hyperintense image artifact when it is present, as seen in the magnitude image of a section of bovine liver tissue (Fig. 6a). However, the phase difference during heating was quite stable, and the temperature maps derived from the phase sensitive PRF sequence (Figs. 6b and 6c) were artifact free. Fig. 6b is the temperature map following a heating sequence with RF pulse voltages set to zero (i.e., no heating) but with the needle in place as seen in the magnitude image. The heating sequence was repeated with nonzero RF voltage, yielding a localized hyperintense region in the temperature map (Fig. 6c) at the needle tip. The tissue temperature increase measured by MR, 20°C, agrees well with the 22°C temperature increase reported by the fiber optic sensor in the needle tip.

C. Phantom testing

Wire pickup—Temperature-time profiles for various wire lengths at 1.5 T are shown in Fig. 7a. Heating was strongly affected by the wire length, with wire lengths close to the resonant length yielding the greatest heating rate, which we define as the initial rate of temperature increase. At 3.0 T, the length difference between minimum and maximum heating rate was roughly half that at 1.5 T, in accord with the shortened wavelength at the higher frequency. Because the wavelength associated with the wire varies with position, and is thus not well-defined, a clear sinusoidal variation of heating rate with length was not observed. The non-monotonic increase in temperature seen in some of the profiles is likely due to arcing, boiling, convection, charring (eschar formation), corrosion, and gel compositional changes at the wire tip, which damage the exposed wire surface, alter its contact resistance and lead to unsteady current flow as cycles of insulating material buildup and breakthrough occur at the tip.

Fig. 7b demonstrates that the heating rate is proportional to the RF duty cycle of the pulse sequence (effectively proportional to SAR). The TR of a gradient echo pulse sequence was varied while keeping the flip angle fixed in shape and amplitude to create a varying RF duty cycle. The heating rate was found to be proportional to the duty cycle.

The peak RF voltage of the pulse at fixed TR was also varied while the heating rate was measured (Fig. 7c). The increase in the heating rate with RF voltage is roughly between linear and quadratic. This could be due to random error in the measurement, or due to the limited range of available RF power to map out a clear relationship.

Loop pickup—The temperature profiles for the loop pickups are shown in Fig. 7d. The larger, 19 cm × 19 cm, loop yielded greater heating, reaching a temperature of ~75°C in ~18 seconds, in contrast to the 47°C reached by the smaller, 11 cm × 11 cm loop in the same period of time. This is in accord with Eqs. (2) and (3) (larger integrals result from longer pickup coil perimeters), and with the simplified formulation of Faraday’s law for a loop (the EMF is proportional to the loop area).

D. Bovine liver tissue

The conventional ablation system required approximately 3.5 minutes to yield the thermal lesion shown in Fig. 8a. The lesion appears elliptical because of the slant of the RFA needle, and is about 5 mm in diameter measured transversely. MR-RFA produced a similar lesion of about 4 mm (Fig. 8b) in 1–2 min. The longitudinal extent of the lesion depends on the exposed wire length. Fig. 8c shows the longitudinal section of an MR-RFA ablation with 20 mm exposed length. MR-RFA applicators with two or four copper needles [45] produced lesions of larger spatial extent in excised liver tissue, but required longer heating time. Unlike the gel, which contains mostly a dilute polysaccharide (agar), tissue contains protein, lipid and many other constituents at high concentration, and is far more susceptible to coagulation and charring than the gel. As a result, the temperature-time profiles in tissue often exhibited a maximum temperature well below the near-100°C temperature achievable with the gel, as well as greater instability once the maximum temperature was reached.

E. Pig cadavers

The thoracic anatomy was visualized with a series of rapid gradient echo scans in the A-P, S-I and R-L directions, permitting the needle to be inserted through the skin of the abdomen just below the lowest right rib and into the liver. The needle artifact in the anatomic scans was used to visualize the tip placement. Multiple placements of the needle followed by ablations were conducted, using the wire pickup. The heating rate was generally lower than with phantoms or sections of liver tissue. This may be due to the very different conditions of the wire geometry. The animal almost filled the bore of the magnet, and the wire ran close to the animal for a considerable distance, likely affecting the transmission line characteristics. Nevertheless, a needle tip temperature of 70°C as measured by the fiber optic sensor was achieved, and thermal lesions of the order of 1 cm diameter were found in the liver on gross examination.

F. Live pigs

Fig. 9a is a photograph of the anesthetized intubated animal on the patient table outside the magnet immediately after successful placement of the needle (arrow) but before MR-RFA. Images containing the needle tip from the A-P, S-I and R-L anatomic slice stacks are shown in Figs. 9b–d. The needle tip, marked by arrows, was easily distinguishable by its hyperintense signal. The long arrows mark in (a), (c) and (d) mark the approximate direction of the needle track. Fig. 10a shows the entry points of three needle placements (arrows) in the excised liver of the animal from Fig. 9. The right panel of Fig. 10b shows two of the needle tracks and thermal lesions in a sectional view of the liver.

V. DISCUSSION

One of the major benefits of MR-RFA is its inherent integration with the MRI scanner. In addition to facilitating the placement of the RF applicator in the target tissue, it also allows monitoring of the ablation progress in real-time using temperature mapping sequences. Moreover, since ablation causes changes in tissue properties, the actual impact on the tissue (rather than simply its temperature change) can be quantified by sensitizing the scan to the appropriate relaxation mechanism. This is important since, *in vivo*, blood perfusion is highly

effective at removing heat deposited by the RF applicator [46] which considerably reduces the heating efficiency. The ability to apply the therapy with the scanner and monitor the tissue condition could lead to lower tumor recurrence rates by confirming that the tumor has been killed at its margins.

MR-RFA is most similar to MR-guided conventional RFA, the major differences being the elimination of the ground electrode as well as the external RF generator and cables. Using Larmor frequency RF for heating also eliminates the need for electrical filtering of the cables to prevent interference with imaging [47], [48]. The ablation electrode becomes in effect equivalent to a bipolar electrode in that there is no need to manage a separate current return path. Conventional RFA systems (including the Cool-tip system) operate in the range of 375—500 kHz, at which wavelength effects and reactance are irrelevant. The heating is merely a function of current density. At the other extreme, microwave ablation systems, operating in the 915—2450 MHz ranger, are bipolar because the RF energy must be guided to the tissue via a coaxial cable at the end of which the two electrodes must be in close proximity. Although wavelength effects tend to be most important at microwave frequencies, the microwave energy is confined within the coaxial transmission line and only a small volume of tissue, reducing the practical effects of wavelength at microwave frequencies. In this first study, MR-RFA appears to be more efficient (that is, in terms of the ability to reach a kill temperature in a short time) than conventional RFA. As in MR-RFA, microwave ablation systems exhibit a tuning effect (potentially high impedance mismatch a the needle/tissue boundary) [49].

Because the EMF increases linearly with RF frequency (Eqs. (1) and (6)), heating in MR-RFA will in general increase with static magnetic field, the complicated effects of wavelength notwithstanding. SAR, independent of other factors, tends to rise with frequency. Higher field scanners should therefore provide more effective heating, requiring shorter treatment times, in addition to yielding better image quality in the treatment monitoring due to the increased signal-to-noise ratio. However, the shorter wavelength at higher field might lead to greater sensitivity of heating to wire and needle placement, and increased unwanted heating along the wire where it comes into proximity to the patient.

Thermal imaging with the PRF method relies on the accuracy of the image phase to measure the temperature. Although we demonstrated that the presence of the needle in dead tissue does not affect temperature accuracy, motion artifacts in live subjects cause phase errors which make this method untenable, especially in the abdomen with its respiratory and peristaltic motions. In this report we did not address the effects of either motion or heat-induced susceptibility shifts (sometimes referred to as “B_0 shifts,” which are indistinguishable from chemical shifts). This is an important limitation of the present study. However, there are a number of methods described in the literature for MR thermometry in the presence of motion, or which compensate for heat-induced susceptibility shifts [18]. Finally, it should be noted that tissue temperature is merely a biomarker for predicting cell death; MR cannot directly detect the disruption of cellular metabolic activity that leads to cell death.

Because the MR-RFA device is electromagnetically coupled to the body RF coil, it acts as a local receive coil during signal acquisition. As a result, the needle appears prominently in images if the body coil is used for reception, providing a convenient means for its visualization and tracking. The bright region surrounding the wire has the largest cross section where the wire enters the phantom or tissue, reflecting the fact that although the voltage along the wire is largest at the tip, the peak of the current standing wave will occur away from the tip. By reciprocity, the maximum receptivity of the wire acting as a receiver will in general not occur at the tip. Because the RF energy is delivered by this electromagnetic coupling, which is inherently variable, the efficiency will vary among patients and between positions of the RFA needle.

The simulations indicate that the strongest heating occurs in close proximity to the device tip when it is immersed in a homogeneous medium. However, it is possible that hotspots can occur in other, unintended, locations as well. In contrast to the homogeneous phantom used in the simulations and the gel experiments, the human body is composed of multiple tissue types in complex structures. These might contain a low impedance (high current) path or a resonant dielectric structure leading to unwanted heating. To establish the safety of MR-RFA, detailed simulations with a human body model and extensive animal testing will be required in future work. Nevertheless, given that most of the heating is confined to a small region near the wire, in conjunction with the fact that the wire tends to detune the transmit coil, the global SAR, computed across the entire body, is likely to be reduced. The SAR reported by the scanner would therefore overestimate the global SAR in the patient yielding a built-in safety margin. However, because overall SAR to the patient must be limited to FDA guidelines, the RF applicator must be highly efficient so that relatively low SAR sequences can be used. This requires careful tuning of the wire's length to the resonant frequency in order to maximize the power delivered to the target. This might be accomplished via simple trial and error by monitoring the initial heating rate and adjusting the series capacitor accordingly. The anatomic and thermal sequences imposed low SAR values of a few percent, yielding modest temperature rises at the needle of at most a few degrees as measured with the fiber optic sensor, which would not constitute ablation. It is unlikely that MR-RFA would put the scanner hardware at risk because the body RF coil is only modestly detuned according to the simulations, and the scanner RF fault monitor did not trip during experiments.

The porcine model used in this study is often used for liver ablation modeling [45], [49]. The heating of appropriately designed conductive structures in the RF field of an MRI scanner offers significant potential for a novel means of treating tumors by radiofrequency ablation. By dispensing with a separate RF generator, the grounding pad, and external connecting cables, the safety of RF ablations may be improved. The successful *in vivo* ablation of liver tissue on a clinical MRI scanner shown here demonstrates the clinical potential of MR-RFA. In particular, the ability to measure tissue temperature during the procedure should result in better outcomes by allowing direct measurement of the temperature of the tumor margins.

Almost all of the tissue heating is limited to the uninsulated tip of the needle. This offers a means to control the ablated volume by varying the exposed length with a movable insulating sleeve. Heating can also be controlled or effectively stopped by detuning the

pickup device or disconnecting the needle by either mechanical or electronic means. Detuning the wire during imaging would reduce the artifact in images as well as residual heating effects.

The wire and tuned loop RF pickup devices are alternative configurations for coupling RF energy to the needle. The wire is by far the simplest and cheapest pickup device, and can be considered disposable. However, a simple wire trimmed to an appropriate length was typically insufficient to insure adequate heating, and required the insertion of a series variable capacitor that was adjusted to optimize heating. The loop generally provided a higher level of RF energy and reduced somewhat the effect of wire positioning on heating, but also required some adjustment in tuning and positioning. At this stage of the research it is not possible to state definitively which configuration is preferred. With either pickup device, it was possible to achieve adequate heating.

The TSE pulse sequence was used for heating because it was convenient to set its parameters to reach the SAR limit to maximize the RF heating. Other than SAR, the sequence parameters are irrelevant unless it is being used to capture an image. A custom sequence without gradients would serve just as well and would be silent. The heating sequence, if also used for imaging, might result in an image with higher than normal artifact content because tissue parameters in the heated region might be changing during the course of the scan.

VI. CONCLUSION

We have described an RF ablation method, magnetic resonance mediated radiofrequency ablation or MR-RFA, that does not require an external RF generator. The heat energy extracted from the RF field of the scanner using typical clinical pulse sequences is sufficient to ablate tissues and can be controlled using the pulse sequence parameters. The use of the MRI scanner enables guidance for needle placement, and allows for the possibility of intraprocedural imaging of tissue temperature, perfusion, coagulation and other parameters to assess tissue condition.

Acknowledgments

This work was supported by U.S. National Institutes of Health grants R21EB007792 and R44CA203276. Scanner and facilities support was provided in part by National Institutes of Health grant P41EB015896. We thank Dr. Debra Gervais for performing conventional RF ablations on a liver specimen, Daniel Ackerman and Martin Polak for assisting with data analysis, and John Kyum Lee for assisting with software.

References

1. Hue Y-K, Ackerman JL, Nevo E. Novel body coil driven radio frequency ablation device. presented at the Joint Annual Meeting, International Society of Magnetic Resonance in Medicine and European Society for Magnetic Resonance in Medicine and Biology, Stockholm, Sweden. 2010:1819.
2. Cohen O, Zhao M, Nevo E, Zurkiya O, González RG, Yoo AJ, Ackerman JL. Endovascular embolization of aneurysms by interventional MR coagulation. J Vasc Interv Radiol JVIR, vol. 2015; 2(26):S5.
3. Cohen O, Zhao M, Nevo E, Ackerman JL. MR coagulation: a novel minimally invasive approach to aneurysm repair. J Vasc Interv Radiol JVIR. 2017:1–7. in press.

4. Goldberg SN, Gazelle GS, Mueller PR. Thermal ablation therapy for focal malignancy: a unified approach to underlying principles, techniques, and diagnostic imaging guidance. Am J Roentgenol. 2000; 174(2):323–331. [PubMed: 10658699]
5. Rhim H, Goldberg SN, Dodd GD, Solbiati L, Lim HK, Tonolini M, Cho OK. Essential techniques for successful radiofrequency thermal ablation of malignant hepatic tumors. Radiographies. 2001; 21(suppl_1):S17–S35.
6. Breen MS, Breen M, Butts K, Chen L, Saidel GM, Wilson DL. MRI-guided thermal ablation therapy: Model and parameter estimates to predict cell death from MR thermometry images. Ann Biomed Eng. 2007; 35(8):1391–1403. [PubMed: 17436111]
7. Goldberg S, Solbiati L, Gazelle G, Tanabe K, Compton C, Mueller P. Treatment of intrahepatic malignancy with radio-frequency ablation: radiologic-pathologic correlation in 16 patients. AJR. 1997; 168:121.
8. Thomsen S. Pathologic analysis of photothermal and photomechanical effects of laser-tissue interactions. Photochem Photobiol. 1991; 53(6):825–835. [PubMed: 1886941]
9. Rosenthal D, Alexander A, Rosenberg A, Springfield D. Ablation of osteoid osteomas with a percutaneously placed electrode: a new procedure. Radiology. 1992; 183(1):29–33. [PubMed: 1549690]
10. Curley SA, et al. Radiofrequency ablation of unresectable primary and metastatic hepatic malignancies. Ann Surg. Jul 1.1999 230(1)
11. Elias D, Debaere T, Muttillo I, Cavalcanti A, Coyle C, Roche A. How I do it: Intraoperative use of radiofrequency treatment allows an increase in the rate of curative liver resection. J Surg Oncol. 1998; 67(3):190–191. [PubMed: 9530891]
12. Goldberg S, Solbiati L, Hahn P, Cosman E, Conrad J, Fogle R, Gazelle G. Large-volume tissue ablation with radio frequency by using a clustered, internally cooled electrode technique: Laboratory and clinical experience in liver metastases. Radiology. 1998; 209(2):371–379. [PubMed: 9807561]
13. Gervais DA, McGovern FJ, Wood BJ, Goldberg SN, McDougal WS, Mueller PR. Radio-frequency ablation of renal cell carcinoma: Early clinical experience. Radiology. 2000; 217(3):665–672. [PubMed: 11110926]
14. Wood BJ, Bates S. Radiofrequency thermal ablation of a splenic metastasis. J Vasc Interv Radiol. 2001; 12(2):261–263. [PubMed: 11265893]
15. Lencioni R, et al. Response to radiofrequency ablation of pulmonary tumours: a prospective, intention-to-treat, multicentre clinical trial (the RAPTURE study). Lancet Oncol. 2008; 9(7):621–628. [PubMed: 18565793]
16. Mahnken AH, Tacke JA, Wildberger JE, Günther RW. Radiofrequency ablation of osteoid osteoma: initial results with a bipolar ablation device. J Vasc Interv Radiol. 2006; 17(9):1465–1470. [PubMed: 16990466]
17. Merkle EM, Boll DT, Boaz T, Duerk JL, Chung YC, Jacobs GH, Varnes ME, Lewin JS. MRI-guided radiofrequency thermal ablation of implanted VX2 liver tumors in a rabbit model: Demonstration of feasibility at 0.2 T. Magn Reson Med. 1999; 42(1):141–149. [PubMed: 10398960]
18. Rieke V, Pauly K Butts. MR thermometry. J Magn Reson Imaging JMRI. Feb; 2008 27(2):376–390. [PubMed: 18219673]
19. Weidensteiner C, Quesson B, Caire-Gana B, Kerioui N, Rullier A, Trillaud H, Moonen CT. Real-time MR temperature mapping of rabbit liver in vivo during thermal ablation. Magn Reson Med. 2003; 50(2):322–330. [PubMed: 12876709]
20. Lepetit-Coiffé M, Quesson B, Seror O, Dumont E, Le Bail B, Moonen CT, Trillaud H. Real-time monitoring of radiofrequency ablation of rabbit liver by respiratory-gated quantitative temperature MRI. J Magn Reson Imaging. 2006; 24(1):152–159. [PubMed: 16767739]
21. Kelekis AD, Terraz S, Roggan A, Terrier F, Majno P, Mentha G, Roth A, Becker CD. Percutaneous treatment of liver tumors with an adapted probe for cooled-tip, impedance-controlled radio-frequency ablation under open-magnet MR guidance: initial results. Eur Radiol. 2003; 13(5): 1100–1105. [PubMed: 12695834]

22. Clasen S, Boss A, Schmidt D, Schraml C, Fritz J, Schick F, Claussen CD, Pereira PL. MR-guided radiofrequency ablation in a 0.2-T open MR system: Technical success and technique effectiveness in 100 liver tumors. J Magn Reson Imaging. 2007; 26(4):1043–1052. [PubMed: 17896364]
23. Laumonier H, Blanc J-F, Quesson B, Seror O, Laurent C, Bioulac-Sage P, Balabaud C, Trillaud H. Real-time monitoring of hepatocellular carcinoma radiofrequency ablation by quantitative temperature MRI. Seminars in Liver Disease. 2006; 26:391. [PubMed: 17051453]
24. Schutt DJ, Haemmerich D. Sequential activation of a segmented ground pad reduces skin heating during radiofrequency tumor ablation: Optimization via computational models. IEEE Trans Biomed Eng. Jul; 2008 55(7):1881–1889. [PubMed: 18595807]
25. Bleicher RJ, Allegra DP, Nora DT, Wood TF, Foshag LJ, Bilchik AJ. Radiofrequency ablation in 447 complex unresectable liver tumors: Lessons learned. Ann Surg Oncol. Jan; 2003 10(1):52–58. [PubMed: 12513961]
26. Goette A, Reek S, Klein HU, Geller JC. Case report: Severe skin burn at the site of the indifferent electrode after radiofrequency catheter ablation of typical atrial flutter. J Interv Card Electrophysiol. Sep; 2001 5(3):337–340. [PubMed: 11500589]
27. Steinke K, Gananadha S, King J, Zhao J, Morris DL. Dispersive pad site burns with modern radiofrequency ablation equipment. Surg Laparosc Endosc Percutan Tech. Dec; 2003 13(6):366–371. [PubMed: 14712096]
28. Huffman SD, Huffman NP, Lewandowski RJ, Brown DB. Radiofrequency ablation complicated by skin burn. Semin Interv Radiol. Jun; 2011 28(2):179–182.
29. Brace CL, Laeseke PF, Sampson LA, Frey TM, Mukherjee R, Lee FT. Radiofrequency ablation with a high-power generator: Device efficacy in an in vivo porcine liver model. Int J Hyperthermia. Jan; 2007 23(4):387–394. [PubMed: 17558738]
30. Cady B, et al. Surgical margin in hepatic resection for colorectal metastasis: a critical and improvable determinant of outcome. Ann Surg. 1998; 227(4):566. [PubMed: 9563547]
31. Abdalla EK, Vauthey J-N, Ellis LM, Ellis V, Pollock R, Broglio KR, Hess K, Curley SA. Recurrence and outcomes following hepatic resection, radiofrequency ablation, and combined resection/ablation for colorectal liver metastases. Ann Surg. Jun; 2004 239(6):818–825. discussion 825-827. [PubMed: 15166961]
32. Sucandy I, Cheek S, Golas BJ, Tsung A, Geller DA, Marsh JW. Longterm survival outcomes of patients undergoing treatment with radiofrequency ablation for hepatocellular carcinoma and metastatic colorectal cancer liver tumors. HPB. Sep; 2016 18(9):756–763. [PubMed: 27593593]
33. Clasen S, Rempp H, Boss A, Schmidt D, Fritz J, Schraml C, Schick F, Claussen CD, Pereira PL. MR-guided radiofrequency ablation of hepatocellular carcinoma: long-term effectiveness. J Vasc Interv Radiol JVIR. Jun; 2011 22(6):762–770. [PubMed: 21530311]
34. Postma EL, van Hillegersberg R, Daniel BL, Merckel LG, Verkooijen HM, van den Bosch MAAJ. MRI-guided ablation of breast cancer: where do we stand today? J Magn Reson Imaging JMRI. Aug; 2011 34(2):254–261. [PubMed: 21780220]
35. Leylek AM, Whitman GJ, Vilar VS, Kisilevzky N, Faintuch S. Radiofrequency ablation for breast cancer. Tech Vasc Interv Radiol. Dec; 2013 16(4):269–276. [PubMed: 24238382]
36. Clasen S, Rempp H, Hoffmann R, Graf H, Pereira PL, Claussen CD. Image-guided radiofrequency ablation of hepatocellular carcinoma (HCC): is MR guidance more effective than CT guidance? Eur J Radiol. Jan; 2014 83(1):111–116. [PubMed: 24161781]
37. Gombos EC, Jagadeesan J, Richman DM, Kacher DF. Magnetic Resonance Imaging-Guided Breast Interventions: Role in Biopsy Targeting and Lumpectomies. Magn Reson Imaging Clin N Am. Nov; 2015 23(4):547–561. [PubMed: 26499274]
38. Fleming MM, Holbrook AI, Newell MS. Update on image- guided percutaneous ablation of breast cancer. AJR Am J Roentgenol. Feb; 2017 208(2):267–274. [PubMed: 27762603]
39. Bayin, ŞS. Mathematical Methods in Science and Engineering Hoboken. NJ: Wiley-Interscience; 2006.
40. Pozar, DM. Microwave Engineering. 3rd. Hoboken, NJ: J Wiley; 2005.
41. Gabriel S, Lau RW, Gabriel C. The dielectric properties of biological tissues: II. Measurements in the frequency range 10 Hz to 20 GHz. Phys Med Biol. Nov; 1996 41(11):2251–2269. [PubMed: 8938025]

42. Bernardi P, Cavagnaro M, Pisa S, Piuzzi E. Specific absorption rate and temperature elevation in a subject exposed in the far-field of radio-frequency sources operating in the 10-900-MHz range. Biomed Eng IEEE Trans On. 2003; 50(3):295–304.
43. De Poorter J, De Wagter C, De Deene Y, Thomsen C, Ståhlberg F, Achten E. Noninvasive MRI thermometry with the proton resonance frequency (PRF) method: in vivo results in human muscle. Magn Reson Med. Jan; 1995 33(1):74–81. [PubMed: 7891538]
44. Jenkinson M. Fast, automated, N-dimensional phase-unwrapping algorithm. Magn Reson Med. Jan; 2003 49(1):193–197. [PubMed: 12509838]
45. Chinn SB Jr, Lee FT, Kennedy GD, Chinn C, Johnson CD III, Winter TC, Warner TF, Mahvi DM. Effect of vascular occlusion on radiofrequency ablation of the liver: Results in a porcine model. Am J Roentgenol. 2001; 176(3):789–795. [PubMed: 11222227]
46. Patterson EJ, Scudamore CH, Owen DA, Nagy AG, Buczkowski AK. Radiofrequency ablation of porcine liver in vivo: Effects of blood flow and treatment time on lesion size. Ann Surg. 1998; 227(4):559. [PubMed: 9563546]
47. Zhang Q, Chung YC, Lewin JS, Duerk JL. A method for simultaneous RF ablation and MRI. J Magn Reson Imaging JMRI. Feb; 1998 8(1):110–114. [PubMed: 9500269]
48. Oshiro T, Sinha U, Lu D, Sinha S. Reduction of electronic noise from radiofrequency generator during radiofrequency ablation in interventional MRI. J Comput Assist Tomogr. Apr; 2002 26(2): 308–316. [PubMed: 11884792]
49. Wright AS, Sampson LA, Warner TF, Mahvi DM, Lee FT. Radiofrequency versus microwave ablation in a hepatic porcine model. Radiology. 2005; 236(1):132–139. [PubMed: 15987969]

Significance

MR-RFA may add value to MRI with the addition of a potentially disposable ablation device while retaining MRI's ability to provide real time procedure guidance and measurement of tissue temperature, perfusion and coagulation.

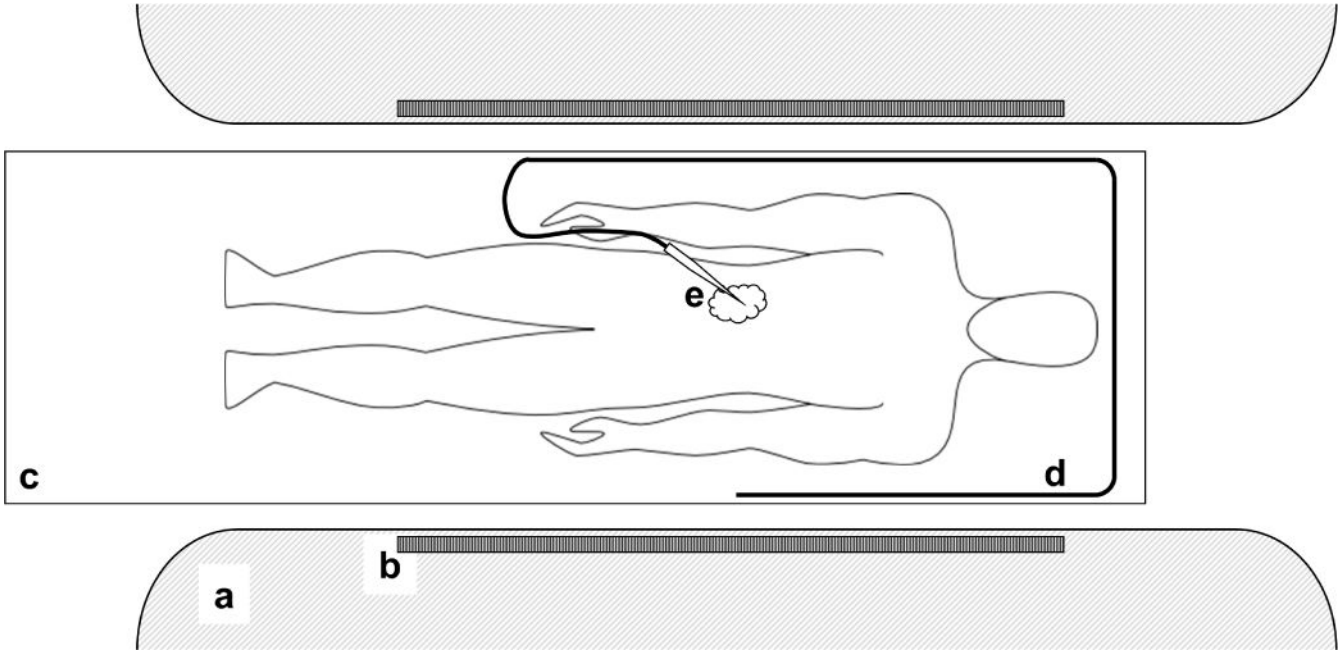

Fig. 1.

Magnetic resonance mediated radiofrequency ablation (MR-RFA) concept. (a) MRI scanner magnet assembly. (b) Body RF coil. (c) Patient table. (d) Long wire RF pickup antenna electromagnetically coupled to body coil. (e) RF needle applicator with tip inserted percutaneously into targeted tumor.

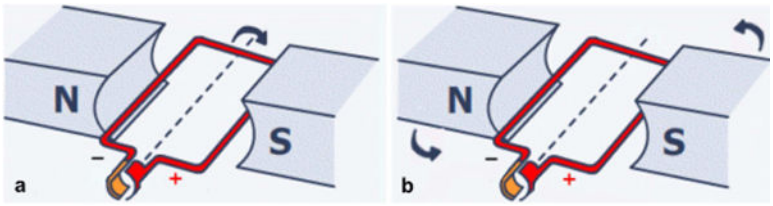

Fig. 2.

Illustration of Faraday's Law of Induction. (a) In typical electric power generation, a rotating wire loop is immersed in a static magnetic field, inducting an EMF along the wire's length. (b) In MR-RFA induction of an EMF occurs likewise when the static wire loop is exposed to a rotating magnetic field.

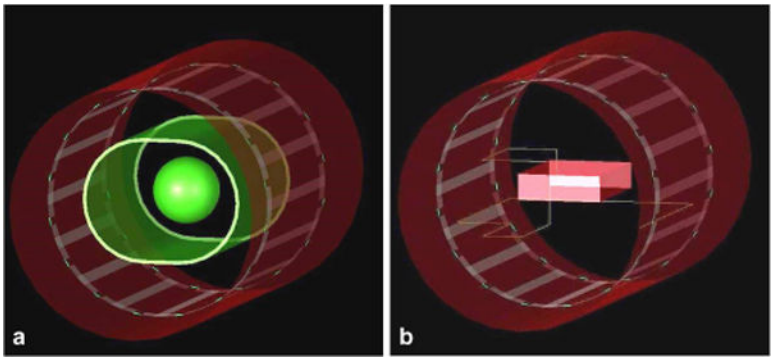

Fig. 3.

Geometry definition of the shielded 16-segment highpass birdcage body RF coil used in numerical simulations of the electric and magnetic fields. (a) Sixty cm long × 60 cm diameter body coil containing Siemens standard body loader. Quadrature drive ports are at the 4:00 and 7:00 o'clock positions. (b) Body coil containing 31 × 23 × 7 cm liver phantom (small rectangular solid) and looped RF pickup wire (thin white line) with one end embedded 4 cm into the liver phantom.

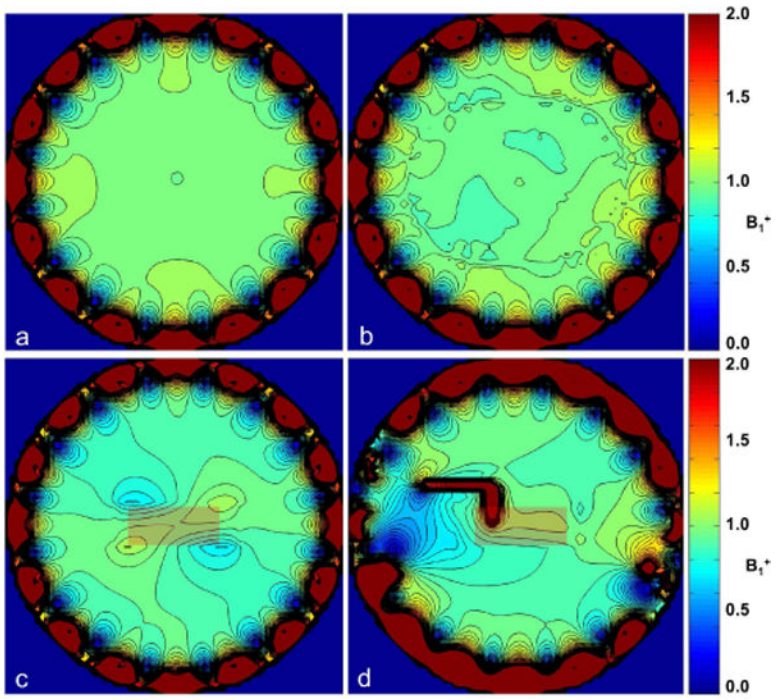

Fig. 4.

Simulated RF magnetic field results in the central plane transverse to the body coil axis. Contour intervals are 5% of the B_1^+ at the center of the unloaded coil; maximum displayed is B_1^+ clipped to 2× this value. (a) Unloaded coil. (b) Body-loaded coil. (c) Coil containing liver phantom but no body loader. (d) Coil containing liver phantom and pickup wire. B_1^+ is significantly enhanced in the immediate vicinity of the wire (above the limit of the color scale). Only two segments including the tip of the wire appear in the displayed central plane. Although the wire is represented in the simulation geometry as an infinitely thin perfect electrical conductor, the spatial extent of the simulation result is defined by the 1-cm computational grid; the wire therefore appears to have a width of at least 2 cm in the plot.

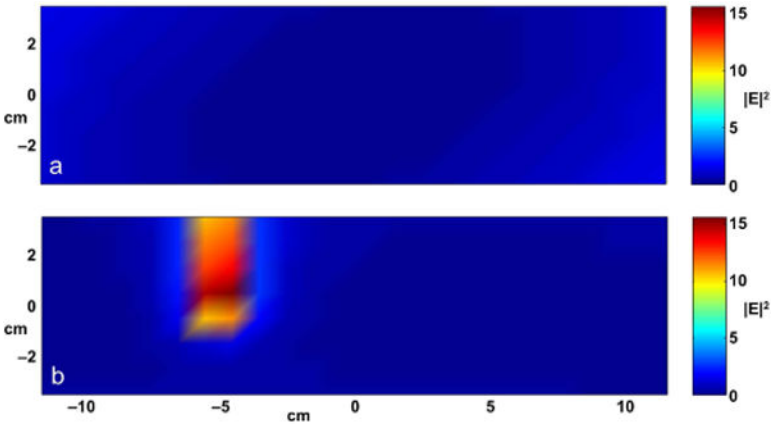

Fig. 5.

Simulated relative SAR in the liver phantom. Each rectangular panel shows the full cross section of the liver phantom; air boundaries are at the edges. (a) No wire present, (b) wire tip immersed 4 cm into the liver. The peak enhancement is 9.7 relative to the liver with no wire present. Because of a slight body coil detuning caused by the wire, the SAR integrated over the liver with the wire present is only 0.44 of the SAR without the wire.

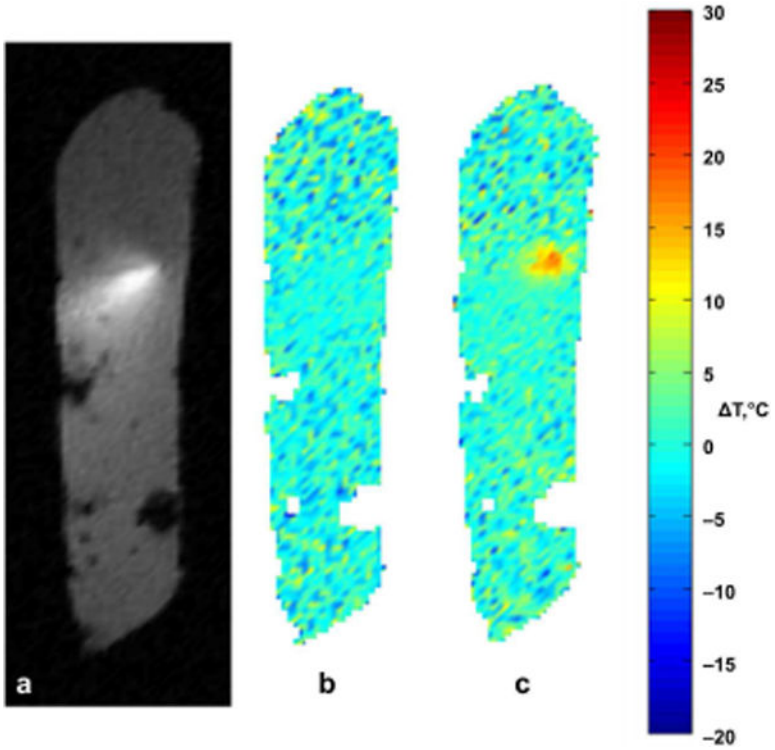

Fig. 6.

MR thermometry during MR-RFA of a slab of excised bovine liver tissue using the proton resonance frequency (PRF) shift method. (a) Magnitude image of the liver. The hyperintense artifact shows the location of the needle tip and can be exploited for tracking the device. (b) Temperature increase during a sham heating period (no RF applied in the heating pulse sequence); although the needle tip creates a significant magnitude image artifact, the image phase near the tip is sufficiently reproducible to eliminate the artifact in the thermal map. (c) Temperature increase during an actual heating period. The peak tissue temperature increase by PRF, about 20°C, agrees well with the 22°C increase recorded by the fiber optic temperature sensor in the needle tip.

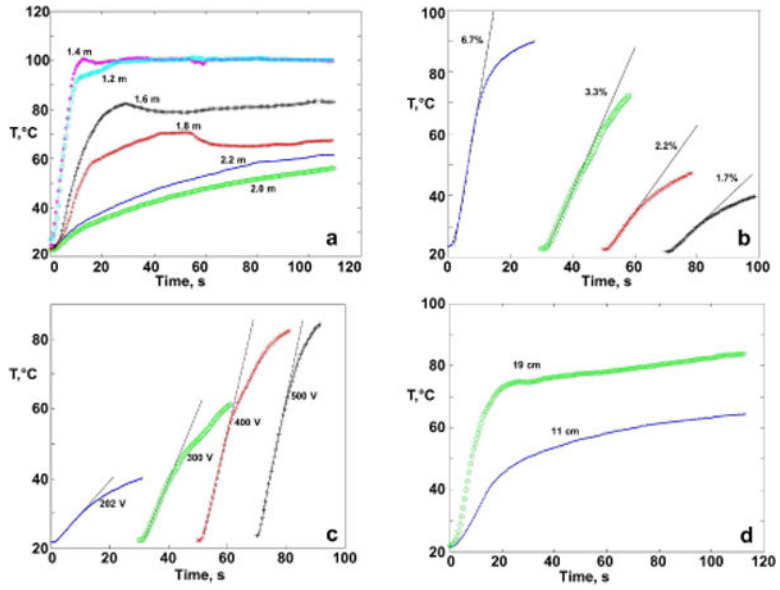

Fig. 7.

Temperature-time profiles of MR-RFA in a doped saline agar gel phantom measured by fiber optic thermometry. Experiments (a–c) used a long wire RF pickup with 5 mm of exposed conductor at the wire tip immersed in the gel. The temperature sensor was affixed near the end of the wire with Teflon tape. Experiment (d) used tuned RF pickup loops coupled to small diameter coaxial cable with 5 mm of exposed center conductor. Curves in (b) and (c) are displaced horizontally in time for clarity. (a) Variation with wire length. The heating rate (initial slope of the temperature vs. time curve) is strongly dependent on the length. The maximum temperature is limited by the boiling point of the gel (about 100°C). At higher heating rates, the asymptotic temperature is unstable because of boiling, convection, and compositional changes at the tip, leading to unstable current flow and temperature. (b) Increase in heating rate with RF duty cycle with fixed amplitude RF heating pulses. (c) Increase in heating rate with RF pulse voltage at fixed RF pulse timing. (d) Heating rate comparison for different RF pickup loop diameters.

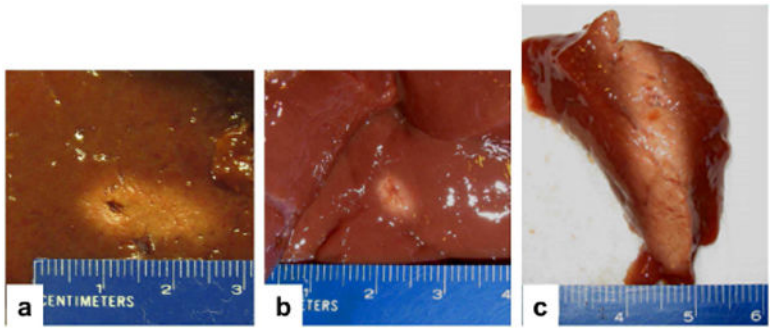

Fig. 8.

Comparison of excised liver tissue ablation lesions between a commercial RFA system and MR-RFA. (a) Lesion created with a commercial RFA generator and needle in about 3.5 min. Elliptical shape is due to the angular insertion of the needle. (b) Lesion created with MR-RFA with 16 gauge bare copper wire needle in about 1–2 min. (c) MR-RFA lesion sectioned parallel to the needle track with 20 mm exposed conductor length.

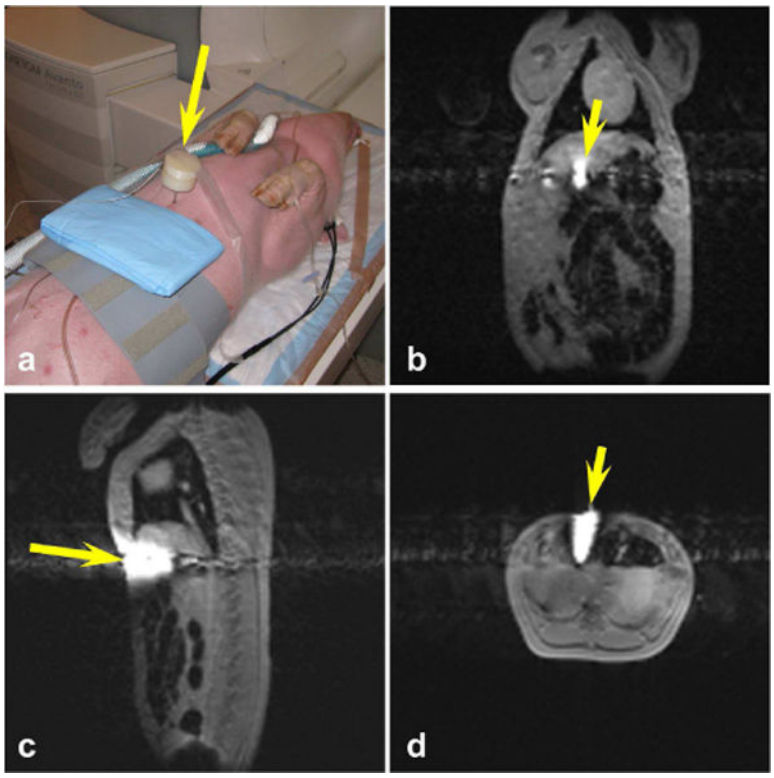

Fig. 9.

MR-RFA in live domestic swine. (a) Photograph of the anesthetized animal on the patient table outside the magnet following MR-RFA needle placement in the liver using MR guidance. The arrow points to the needle handle and is aligned with the needle track. (b) Coronal, (c) sagittal and (d) gradient echo images (uncompensated for motion) confirming needle placement before MR-RFA. The needle tip artifact makes it easily visible. Field of view 500 × 500 mm.

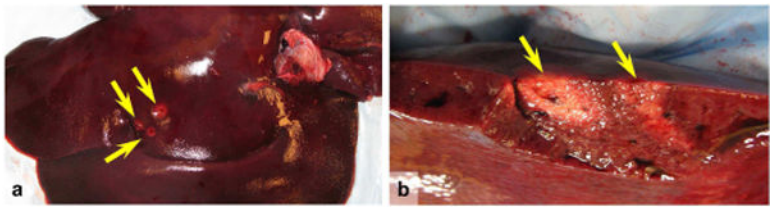

Fig. 10.

Photographs of the post-ablation excised liver from the in vivo MR-RFA procedure. (a) Entry points of three needle placements (arrows). (b) Sectional view capturing two of the needle placements, demonstrating thermal lesions.